

Image-based Separation of Diffuse and Specular Reflections using Environmental Structured Illumination, Supplemental Material

ICT Technical Report ICT-TR-01-2009 (Feb. 2009)

Bruce Lamond Pieter Peers Abhijeet Ghosh Paul Debevec
University of Southern California, Institute for Creative Technologies

Abstract

We present an image-based method for separating diffuse and specular reflections using environmental structured illumination. Two types of structured illumination are discussed: phase-shifted sine wave patterns, and phase-shifted binary stripe patterns. In both cases the low-pass filtering nature of diffuse reflections is utilized to separate the reflection components. We illustrate our method on a wide range of example scenes and applications.

1. Introduction

In this technical report additional results, validations, and detailed theoretical derivations are provided to support [2], and is organized as follows:

- Section 2 and 3 repeats the problem statement and derivation of component separation under the phase-shifted sine wave patterns from [2].
- Section 4 provides an in depth derivation of component separation using the phase-shifted binary stripe patterns.
- Section 5 gives the formal derivation for component separation under user-specified incident illumination.
- Section 6 discusses the influence of the separation pattern frequency.
- Section 7 provides visual comparisons between polarization based separation and our image-based method.
- Section 8 shows additional results.
- Section 9 shows additional results of the photometric stereo and SVBRDF estimation applications.

2. Problem Statement

Given diffuse and specular reflectance functions for each pixel \mathbf{p} and incident lighting directions ω , denoted by $\mathbf{D}(\mathbf{p}, \omega)$ and $\mathbf{S}(\mathbf{p}, \omega)$ respectively, the goal is to compute the specular radiance $\rho_s(\mathbf{p})$, and diffuse radiance $\rho_d(\mathbf{p})$:

$$\rho_d(\mathbf{p}) = \int_{\Gamma} \mathbf{D}(\mathbf{p}, \omega) \bar{\mathbf{I}}(\omega) d\omega, \quad (1)$$

$$\rho_s(\mathbf{p}) = \int_{\Gamma} \mathbf{S}(\mathbf{p}, \omega) \bar{\mathbf{I}}(\omega) d\omega, \quad (2)$$

where $\bar{\mathbf{I}}(\omega)$ is the lighting environment for which the separation is desired, and Γ is the solid angle over which $\bar{\mathbf{I}}(\omega)$ is defined. Unless noted differently we will assume $\Gamma = \Omega$ (the full sphere of incident lighting directions), and $\bar{\mathbf{I}}(\omega) = 1$.

In this report we will compute $\rho_d(\mathbf{p})$, and $\rho_s(\mathbf{p})$ from a few observations $\mathbf{E}_i(\mathbf{p})$ of a scene taken from a fixed vantage point under different controlled distant environmental illumination conditions \mathbf{I}_i . Ignoring inter-reflections, and occlusions, the observed radiance $\mathbf{E}_i(\mathbf{p})$ under the i -th illumination condition \mathbf{I}_i is governed by:

$$\mathbf{E}_i(\mathbf{p}) = \int_{\Gamma} (\mathbf{D}(\mathbf{p}, \omega) + \mathbf{S}(\mathbf{p}, \omega)) \mathbf{I}_i(\omega) d\omega, \quad (3)$$

The presented method will compute $\rho_d(\mathbf{p})$ and $\rho_s(\mathbf{p})$ for each pixel without using information from other pixels. Therefore, we drop the reference to a specific pixel \mathbf{p} for notational simplicity.

3. Phase-shifted Sine Wave Patterns

Let us define different sine wave illumination patterns, each with a fixed frequency f , but with different phases φ_i : $\sin(f\phi + \varphi_i)$, with $\omega = (\theta, \phi)$, and $d\omega = \sin(\theta)d\theta d\phi$. The specific orientation of the azimuthal angle ϕ and polar

angle θ does not matter, as long as they are consistently chosen. Note that these sine wave patterns are constant over θ . In order to obtain a physically realizable illumination condition, we add a constant offset, such that the complete illumination condition has positive values everywhere: $\mathbf{I}_i(\omega) = \sin(f\phi + \varphi_i) + 1$. Inserting this into Equation (3) gives:

$$\mathbf{E}_i = \int_{\Gamma} (\mathbf{D}(\omega) + \mathbf{S}(\omega)) (\sin(f\phi + \varphi_i) + 1) d\omega. \quad (4)$$

Since \mathbf{I}_i is independent of θ , we include the integration over θ into the definition of \mathbf{D} , and \mathbf{S} , and focus on the integration over ϕ . This yields:

$$\begin{aligned} \mathbf{E}_i &= \rho_d + \rho_s + \int_{\Gamma} \mathbf{D}(\phi) \sin(f\phi + \varphi_i) d\phi \\ &+ \int_{\Gamma} \mathbf{S}(\phi) \sin(f\phi + \varphi_i) d\phi. \end{aligned} \quad (5)$$

If the frequency f is large enough, then the third term is approximately zero [3]. The fourth term can be written as:

$$\begin{aligned} &\int_{\Gamma} \mathbf{S}(\phi) \sin(f\phi + \varphi_i) d\phi \\ &= \int_{\Gamma} \mathbf{S}(\phi) (\sin(f\phi) \cos(\varphi_i) + \cos(f\phi) \sin(\varphi_i)) d\phi \quad (6) \\ &= (\cos(\varphi_i)S + \sin(\varphi_i)C), \end{aligned} \quad (7)$$

where S and C are constants only dependent on the specific form of the specular reflectance function $\mathbf{S}(\cdot)$. Equation (7) defines a phase-shifted sine wave, with the phase directly related to the reflected view-direction and the surface normal. The amplitude of this sine wave corresponds to the magnitude of the f -th frequency component of $\mathbf{S}(\cdot)$. For sufficiently sharp specular reflections, and f low enough, the f -th frequency component is approximately ρ_s , and thus the sine wave defined by Equation (7) reaches its maximum amplitude ρ_s for some φ_{peak} .

Putting this all together yields:

$$\begin{aligned} \mathbf{E}_{peak} &\approx \rho_d + 2\rho_s, \\ \mathbf{E}_{peak+\pi} &\approx \rho_d. \end{aligned} \quad (8)$$

It is, however, unlikely that one of the phases φ_i equals exactly φ_{peak} , and thus \mathbf{E}_{peak} is almost never directly observed. However, φ_{peak} can be computed from any collection of three phases φ_i . Given three observations \mathbf{E}_i of the scene under phase-shifted sine waves with phases $\varphi_i, i \in \{0, 1, 2\}$, we can compute ρ_s and ρ_d as follows. Each observation is of the following form:

$$\mathbf{E}_i = \rho_d + \rho_s + (\cos(\varphi_i)S + \sin(\varphi_i)C). \quad (9)$$

We can write this equation as a linear system with three unknowns A , S and C : $\mathbf{E}_i = A + \cos(\varphi_i)S + \sin(\varphi_i)C$, where $A = \rho_d + \rho_s$. If we have three or more linearly independent observations (e.g., with phases 0, 60 and 120 degrees), then all three unknowns can be computed by solving the linear system, or a linear least squares when more than three observations are made (e.g., for robustness). From this it can be easily shown that:

$$\begin{aligned} \rho_d &\approx A - \sqrt{S^2 + C^2}, \\ \rho_s &\approx \sqrt{S^2 + C^2}. \end{aligned} \quad (10)$$

Note that this approach is similar to phase shifting in structured light-based surface reconstruction [1, 4].

4. Phase-shifted Binary Stripe Patterns

This section gives a detail derivation of separation under the binary stripe patterns. Define a set of phase-shifted binary stripe patterns as:

$$\mathbf{I}_i(\omega) = \Psi\left(\frac{f\phi + \varphi_i}{2\pi}\right) + 1, \quad (11)$$

with $\varphi_i = \frac{2\pi}{nf}i$, n the number of illumination patterns, and:

$$\Psi(x) = \begin{cases} +1 & \text{if } x - [x] \in [0, 0.5) \\ -1 & \text{if } x - [x] \in [0.5, 1). \end{cases} \quad (12)$$

Inserting these patterns into Equation (3), allows us to write the observed radiance similarly to Equation (5):

$$\begin{aligned} \mathbf{E}_i &= \rho_d + \rho_s + \int_{\Gamma} \mathbf{D}(\phi) \Psi\left(\frac{f\phi + \varphi_i}{2\pi}\right) d\phi \\ &+ \int_{\Gamma} \mathbf{S}(\phi) \Psi\left(\frac{f\phi + \varphi_i}{2\pi}\right) d\phi. \end{aligned} \quad (13)$$

As before, we would like to impose conditions on \mathbf{I}_i such that the third term—the integral over the diffuse reflectance function—is approximately zero. A frequency analysis of $\Psi\left(\frac{f\psi + \varphi_i}{2\pi}\right)$ reveals that this function only interacts with frequencies that are odd multiples of f . Exploiting the low-pass behavior of diffuse reflectance functions, and setting a lower bound of $f > 10$, the desired effect is obtained.

As with the phase-shifted sine wave patterns, we would like the fourth term in Equation (13) to reach ρ_s at its peak, and $-\rho_s$ at its minimum. Due to the discrete nature of $\Psi(\cdot)$,



Figure 1. The effect of changing frequencies in the illumination patterns on separated components. The specular component (third and fourth column) has been brightened 8 times. The frequency of patterns ranges from (top to bottom) $\frac{\pi}{175}$, $\frac{\pi}{87}$, $\frac{\pi}{58}$, $\frac{\pi}{22}$ and $\frac{\pi}{11}$ respectively.

it is not possible to interpolate this as before from a limited number of observations, unless additional assumptions on the nature of the specular reflectance function $\mathbf{S}(\cdot)$ are made. In our case we will assume that for at least one of the observed integrals the peak value is exactly reached, and that similarly for at least one observation the minimum value is exactly reached. This implies that the width of the specular lobe covers less than $\frac{\pi}{f} \frac{n-1}{n}$, and thus:

$$\rho_s = \max_i \left(\int_{\Gamma} \mathbf{S}(\phi) \Psi \left(\frac{f\phi + \varphi_i}{2\pi} \right) d\phi \right), \quad (14)$$

$$-\rho_s = \min_i \left(\int_{\Gamma} \mathbf{S}(\phi) \Psi \left(\frac{f\phi + \varphi_i}{2\pi} \right) d\phi \right). \quad (15)$$

Combining this with Equation (13) now gives:

$$\rho_d \approx \min_i \mathbf{E}_i, \quad (16)$$

$$\rho_s \approx \frac{1}{2} \left(\max_i \mathbf{E}_i - \min_i \mathbf{E}_i \right). \quad (17)$$

5. User-specified Environmental Illumination

This section gives a detailed derivation of separation under user-specified environment illumination.

Formally, given some user selected illumination condition $\bar{\mathbf{I}}$, and a set of phase-shifted binary stripe patterns $\mathbf{I}_i, i \in \{0, \dots, n-1\}$, the desired separation is a diffuse component: $\rho_d = \int_{\Gamma} \mathbf{D}(\omega) \bar{\mathbf{I}}(\omega) d\omega$, and a specular component: $\rho_s = \int_{\Gamma} \mathbf{S}(\omega) \bar{\mathbf{I}}(\omega) d\omega$. Now define n novel illumination conditions $\mathbf{I}'_i(\omega) = \bar{\mathbf{I}}(\omega) \mathbf{I}_i(\omega)$, where $\mathbf{I}_i(\omega)$ are the phase-shifted stripe patterns with frequency f and phase φ_i . Replacing \mathbf{I}_i in Equation (3) by \mathbf{I}'_i gives the familiar four term equation for the observed radiance:

$$\mathbf{E}_i = \int_{\Gamma} (\mathbf{D}(\omega) + \mathbf{S}(\omega)) \mathbf{I}'_i(\omega) d\omega, \quad (18)$$

$$\begin{aligned} &= \int_{\Gamma} \mathbf{D}(\omega) \bar{\mathbf{I}}(\omega) d\omega + \int_{\Gamma} \mathbf{S}(\omega) \bar{\mathbf{I}}(\omega) d\omega \\ &\quad + \int_{\Gamma} \mathbf{D}(\omega) (\mathbf{I}'_i(\omega) - \bar{\mathbf{I}}(\omega)) d\omega \\ &\quad + \int_{\Gamma} \mathbf{S}(\omega) (\mathbf{I}'_i(\omega) - \bar{\mathbf{I}}(\omega)) d\omega, \end{aligned} \quad (19)$$

$$\begin{aligned} &= \rho_d + \rho_s + \int_{\Gamma} \mathbf{D}(\omega) (\mathbf{I}'_i(\omega) - \bar{\mathbf{I}}(\omega)) d\omega \\ &\quad + \int_{\Gamma} \mathbf{S}(\omega) (\mathbf{I}'_i(\omega) - \bar{\mathbf{I}}(\omega)) d\omega. \end{aligned} \quad (20)$$

Keeping the same restrictions on the specular reflectance function $\mathbf{S}(\cdot)$ as in Section 4, and defining the solid angle $\alpha = \{\omega | \mathbf{S}(\omega) \neq 0, \omega \in \Gamma\}$, then by definition $\int_{\Gamma} \mathbf{S}(\omega) \mathbf{I}_i(\omega) d\omega = \int_{\alpha} \mathbf{S}(\omega) \mathbf{I}_i(\omega) d\omega$. Furthermore, the

maximum over the fourth term can be approximated by assuming that $\bar{\mathbf{I}}$ does not exhibit high-frequency changes in intensity over a distance $\frac{2\pi}{f}$ for every point in $\bar{\mathbf{I}}$.

$$\begin{aligned} &\max_i \left(\int_{\Gamma} \mathbf{S}(\omega) (\mathbf{I}'_i(\omega) - \bar{\mathbf{I}}(\omega)) d\omega \right) \\ &= \max_i \left(\int_{\alpha} \mathbf{S}(\omega) (\mathbf{I}'_i(\omega) - \bar{\mathbf{I}}(\omega)) d\omega \right), \end{aligned} \quad (21)$$

$$\approx \int_{\alpha} \mathbf{S}(\omega) \bar{\mathbf{I}}(\omega) d\omega = \rho_s. \quad (22)$$

The second step is possible because at least one illumination pattern \mathbf{I}_i is always one in α , and $\bar{\mathbf{I}}$ does not change abruptly over this solid angle. Finally, the third term is approximately zero because of the restriction that $\bar{\mathbf{I}}$ does not change abruptly over a cycle of \mathbf{I}_i .

6. Influence of Illumination Pattern Frequency

Ramamoorthi and Hanrahan [3] showed that the response of a diffuse reflectance function decays quadratically with respect to the frequency of the incident illumination. Therefore, to eliminate the effect of the diffuse reflections as much as possible, we recommend using $f > 10$ as a lower limit. The upper limit for the frequency f depends on the roughness of the specular reflectance function. To illustrate, assume that the specular reflectance function resembles a normalized spherical Gaussian centered around the origin (i.e., the mean of the Gaussian equals zero, and $\rho_s = 1$), and with a small standard deviation (i.e., roughness of the material). Transforming this Gaussian in the frequency domain, yields a new Gaussian, but with a standard deviation *inversely* proportional to the roughness. A mirror-like specular material will have a nearly flat spectrum in the frequency domain with unit magnitude, and any frequency above the lower limit will yield accurate results. A duller specular reflectance function, however, will result in a narrower Gaussian in the frequency domain, and will only be approximately one near the origin. Thus, a low value for f is preferred in order to obtain accurate results. This example illustrates that an upper value for f depends on the roughness of the specular component. Therefore, we argue for selecting a frequency f close to the lower limit as defined before ($f \approx 10$). This is a conservative lower limit that should work in all cases.

Figure 1 illustrates the effects of using different frequency patterns. As can be seen, when the frequency is set too high, much of the specular component is included in the diffuse component. However, when the frequency of the patterns approaches the suggested values of $\frac{\pi}{10}$, the separation converges to the desired separation. Both the stripe and wave patterns perform similarly.

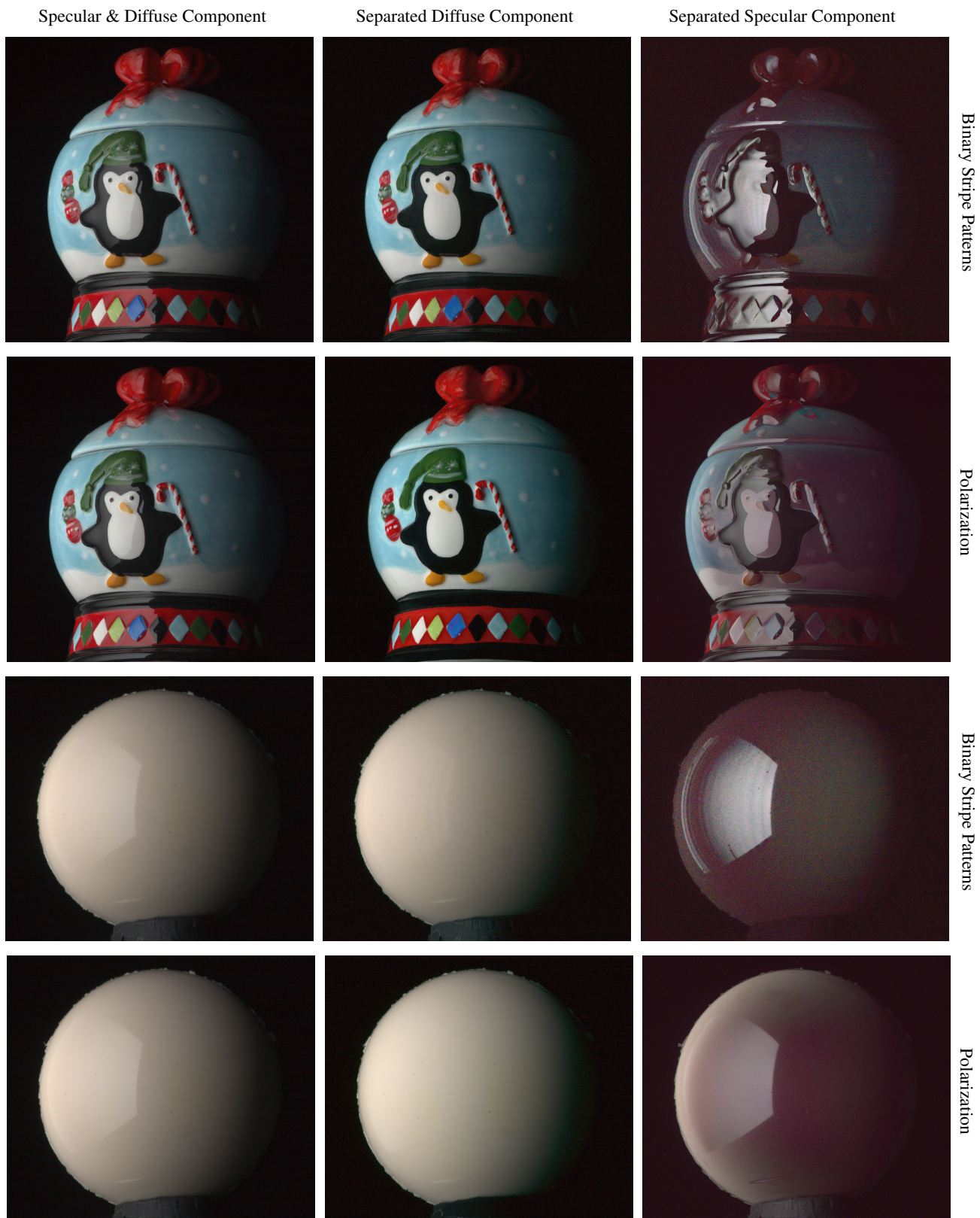


Figure 2. A comparison of polarization based separation versus image-based separation.



Figure 3. Separated components of a US quarter coin. The specular component has been brightened by a factor of two.

7. Validation

We have validated the presented method to a polarization based separation approach. We covered a CRT monitor with a linear polarization sheet. A series of photographs with a differently oriented linear polarizer in front of the camera are captured of the object under constant illumination. Computing the minimum and maximum per pixel yields the cross polarized and parallel polarized photograph of the scene. Additionally, we also compute separations under phase-shifted stripe and sine wave patterns. We calibrate the patterns such that each period covers approximately the same solid angle when viewed from the object.

Figure 2 shows for two objects the separated components obtained using our method and using polarization. For the ceramic object, both results look very similar. There is some specularity left in the image-based diffuse separation on areas with high curvature. For the solid angles seen of the environment through these pixels is larger than a single period of the patterns, and thus the effective frequency of the incident illumination on these pixels is too different to obtain a good separation. Some diffuse light can be also seen leaking into the *polarized* specular component.

The second example is a glossy white ball, a scene that would be impossible to separate using color space methods. As can be seen both methods yield comparable results. There is some banding in the image-based separation due to fluctuations in the brightness of the CRT monitor. Note that the bright stripe on the left of the separated specular component is most likely polarized reflected light from the border of the CRT screen. This line also shows up in the image-based specular separation because this reflection does not follow the desired frequency pattern.

8. Additional Results

Figures 3 and 4 show additional separated results. Some of the components have been artificially brightened for op-

timal viewing. All these examples are captured using the hemispherical reflector outlined in [2].

Figure 3 shows the separation of a US quarter coin. The specular component has been brightened by a factor of two. Note the specular color is different from the light source color.

The top row shows a Rubik's Cube with full illumination (left) separated using high frequency sine wave patterns into diffuse (middle) and specular components (right, brightened 8 times). The high frequency patterns allow invisible fine detail, such as scratches, in the cube surface to be seen in the specular image, while being undetectable in the pre-separated image.

The second row shows an apple exhibiting a glossy shine separated using low-frequency sine waves into diffuse (middle) and specular components (right, brightened 8 times). Near the reflected edges of the hemisphere incomplete separation due to incomplete coverage of the sphere of incident directions can be seen. Such artifacts are more pronounced for glossy reflections than for mirror like specular reflections due to the larger kernel size of these glossy reflectance functions.

The third row shows a human hand with olive oil applied to the visible parts of the left two fingers, and illuminated by full hemispherical illumination, and separated into diffuse (middle) and specular components (right, brightened 16 times) using the binary stripe method. The odd coloration in the specular image is caused by blood moving out of the skin during acquisition. Furthermore note the fine geometrical skin detail visible in the specular image, that is not visible in the other images. As with most organic materials, the diffuse reflections are the result of subsurface scattering which blurs fine geometrical surface details. Specular reflections, on the other hand, are caused by direct surface interactions, and preserve these details.

Finally, the bottom row shows a diffuse tennis ball. The specular images is brightened 128 times. Even at this ex-

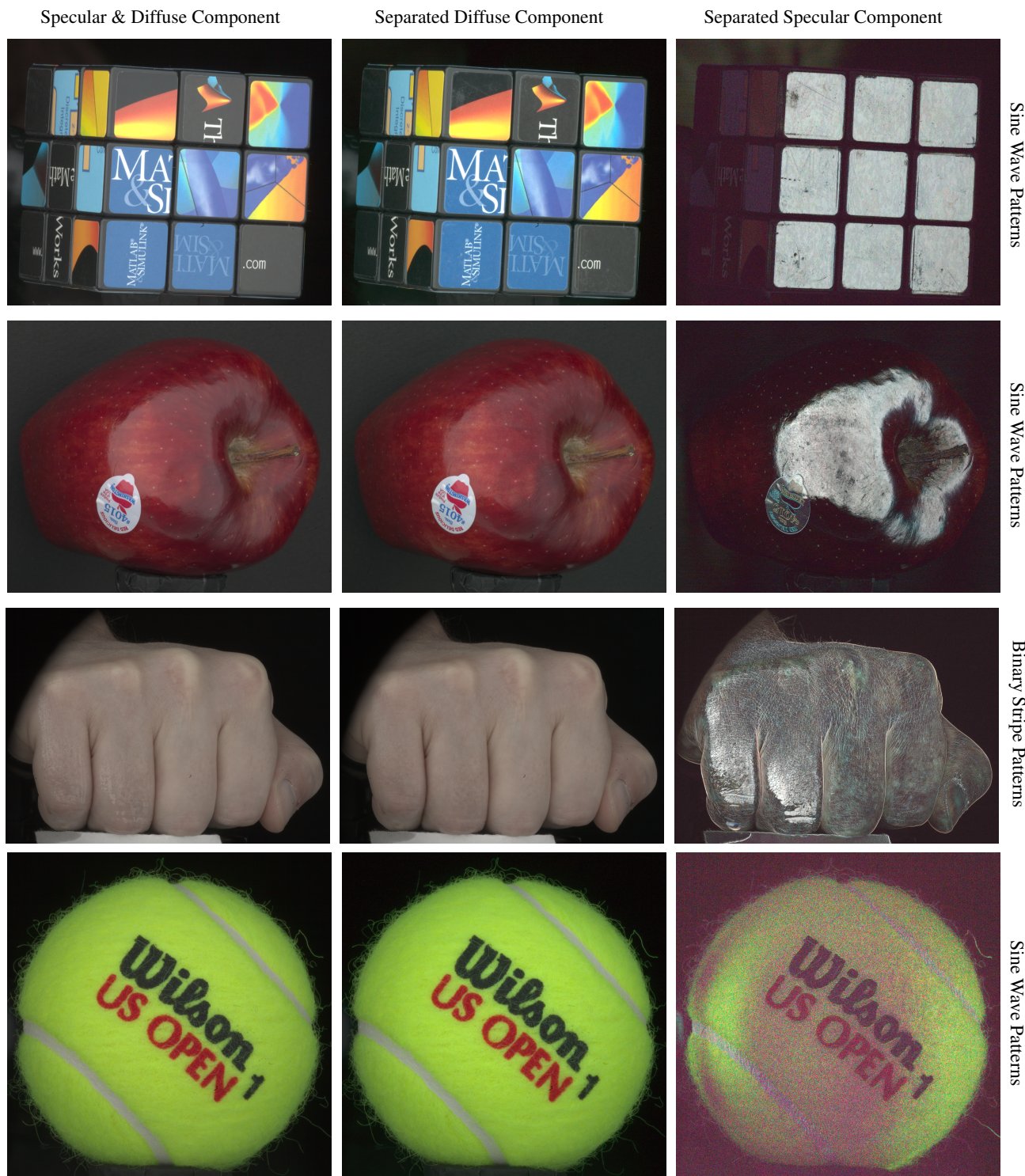


Figure 4. Selection of additional results. Top row: Rubik's Cube with full illumination (left) separated using high frequency sine wave patterns into diffuse (middle) and specular components (right $\times 8$). Second row: Apple separated using low-frequency sine waves into diffuse (middle) and specular components (right $\times 8$). Third row: human hand with olive oil applied to the visible parts of the left 2 fingers. Full illumination separated into diffuse (middle) and specular components (right $\times 16$) using the binary stripe method. Bottom row: a diffuse tennis ball. Note that the noise in the specular image for the diffuse tennis ball is caused by scaling the image $\times 128$ in brightness.

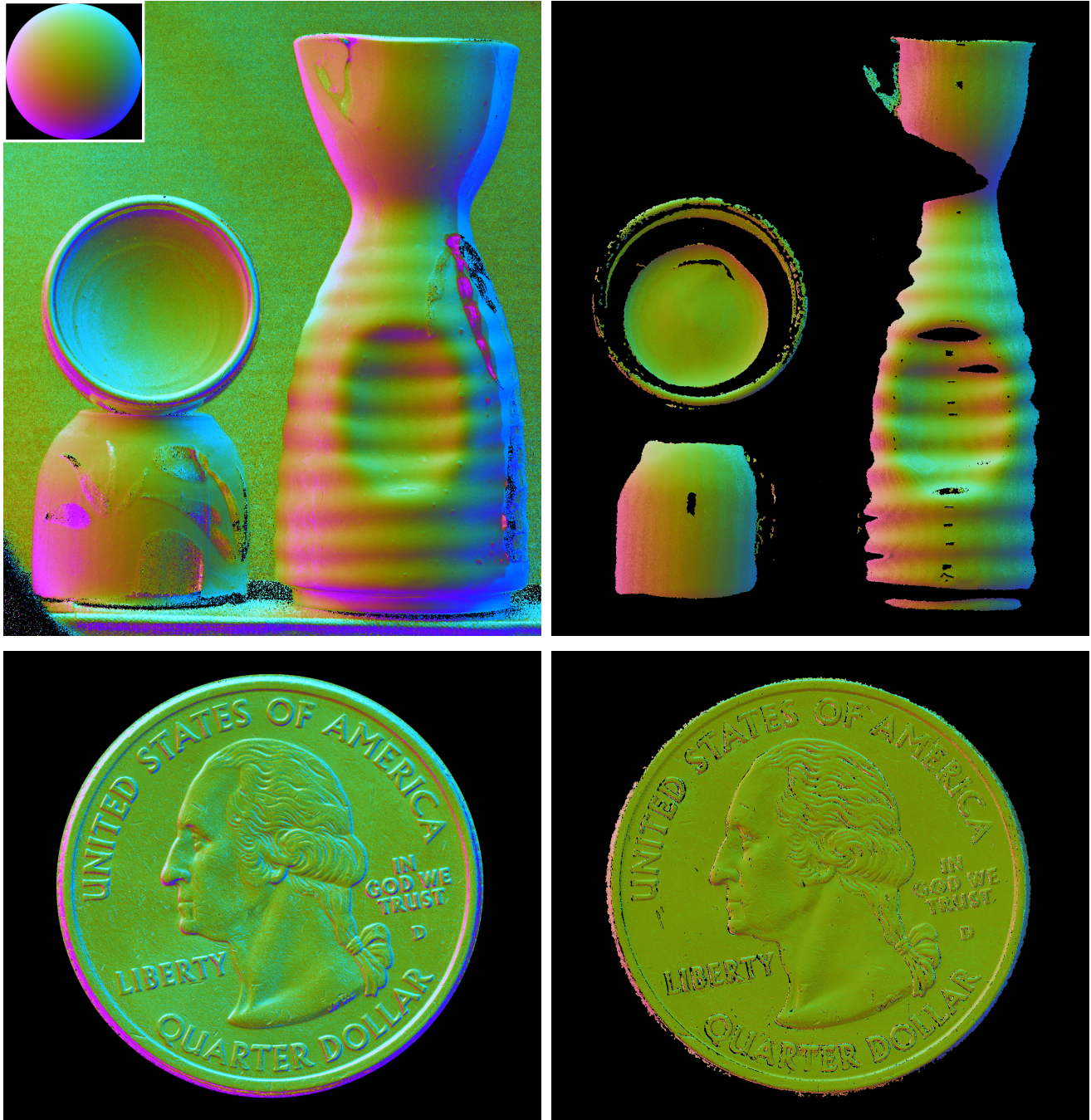


Figure 5. Normals computed from example-based photometric stereo based on the separate diffuse (left) and specular (right) components.

treme, there is hardly any specular reflection visible, illustrating the effectiveness of our method. A very small amount of the diffuse component leaking into the specular component can be observed, because we only illuminate the ball from a hemisphere instead of the full sphere.

9. Additional Application Results

Figure 5 shows an additional photometric normal results. The inset shows the false color coding of normal directions. Note how the scratches on the coin can be seen in the normal maps.

Figure 6 shows additional renderings and visualizations of the SVBRDF sample under different light directions. The

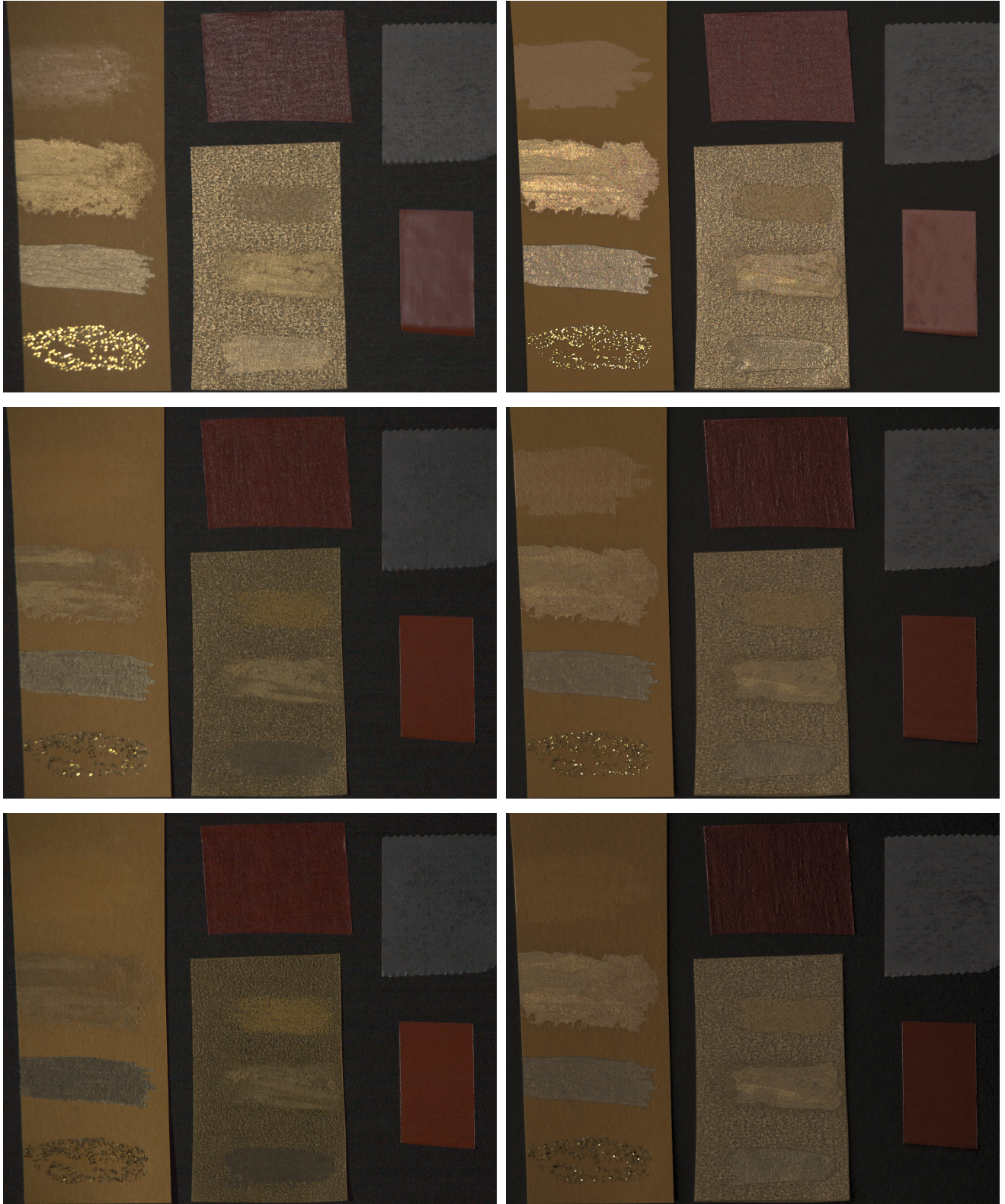


Figure 6. SVBRDF estimated with separated diffuse and specular albedos. **Left:** a reference photograph under a point light source. **Right:** a visualization of fitted SVBRDF parameters under similar lighting conditions.

main differences are due to blooming present around strong highlights in the reference photographs, and the fact that the visualizations use a directional light source which underestimates the true extent of the reference light source used.

Acknowledgments The authors would like to thank Saskia Mordijck, Monica Nicholson, Bill Swartout, Randy Hill, and Randolph Hall for their support and assistance with this work. This work was sponsored by the U.S. Army Research, Development, and Engineering Command (RDE-COM) and the University of Southern California Office of the Provost. The content of the information does not necessarily reflect the position or the policy of the US Government, and no official endorsement should be inferred.

References

- [1] T. Chen, H.-P. Seidel, and H. P. A. Lensch. Modulated phase-shifting for 3d scanning. In *IEEE CVPR*, 2008. 2
- [2] B. Lamond, P. Peers, A. Ghosh, and P. Debevec. Image-based separation of diffuse and specular reflections using environmental structured illumination. In *ICCP*, 2009. 1, 6
- [3] R. Ramamoorthi and P. Hanrahan. The relationship between radiance and irradiance: Determining the illumination from images of a convex lambertian object. In *Journal Opt. Soc. Am.*, 2001. 2, 4
- [4] S. Zhang and S.-T. Yau. Generic nonsinusoidal phase error correction for three-dimensional shape measurement using a digital video projector. *Appl. Opt.*, 46:36–43, 2007. 2